Electrostatic Forces in Field-Perturbed Equilibria

Chem

CellPress

Research Article

Electrostatic forces in field-perturbed equilibria: nanopore analysis of cage complexes

Stefan Borsley, Marius M. Haugland, Samuel Oldknow, James A. Cooper, Michael J. Burke, Aaron Scott, William Grantham, Julia Vallejo, Euan K. Brechin, Paul J. Lusby* and Scott L. Cockroft[1]**

EaStCHEM School of Chemistry, University of Edinburgh, Joseph Black Building, David Brewster Road, Edinburgh EH9 3FJ, U.K.

[1]Lead Contact

*Correspondence: paul.lusby@ed.ac.uk

**Correspondence: scott.cockroft@ed.ac.uk

SUMMARY

Molecular recognition has been widely investigated under equilibrium conditions, but little is known about such processes when perturbed by external forces. Here, we investigate the influence of electric fields on complexes formed between metallosupramolecular cages and a protein nanopore at the single-molecule level. Association rates were dominated by the applied voltage, while local electrostatic interactions between the cage and the nanopore more greatly influenced the dissociation kinetics. Exploiting these principles, it was shown that the externally applied voltage could be used to selectively bind a specific cage from a mixture containing a large excess of other cages. Moreover, the applied voltage could also be used to drive supramolecular enantio-inversion of the chiral cages, or occasionally, the non-equilibrium capture and disassembly of cages deep within the nanopore. Similar principles might be exploited in the design of other molecular devices that operate within externally applied electric fields or biogenic transmembrane potentials.

nanotechnology; single-molecule; nanopore; coordination cages;

INTRODUCTION

Molecular interactions occurring at nanoscale interfaces are crucial in chemistry and biology.[1-6] However, increasing emphasis is placed on escaping thermodynamic equilibrium in synthetic systems;[7,8] life is sustained under non-equilibrium conditions through the consumption of chemical fuels[9-12] and the generation of transmembrane ion potentials.[13] The booming fields of synthetic molecular machines[14-17] and dissipative energy systems[18-21] likewise rely upon the consumption of a chemical fuel or sustained input of energy to maintain the systems under non-equilibrium conditions.[22] However, understanding of the perturbing influence of external forces on equilibria governing recognition processes and the structural dynamics of supramolecular assemblies remains limited due to the challenge of designing suitable systems in which such forces may be systematically varied.[23]

Nanopore sensing typically involves the voltage-driven binding of analytes with a single nanopore under an applied transmembrane potential,[24-27] and thereby provides an excellent opportunity for examining the influence of electric fields on binding equilibria. Notably, the atomically precise structure of the α-hemolysin protein nanopore[28] has been employed for the detection of a wide range of analytes including drugs,[29] chemical weapons,[30] nucleotides[31-33] as well as larger synthetic and biological supramolecular assemblies.[34-36]

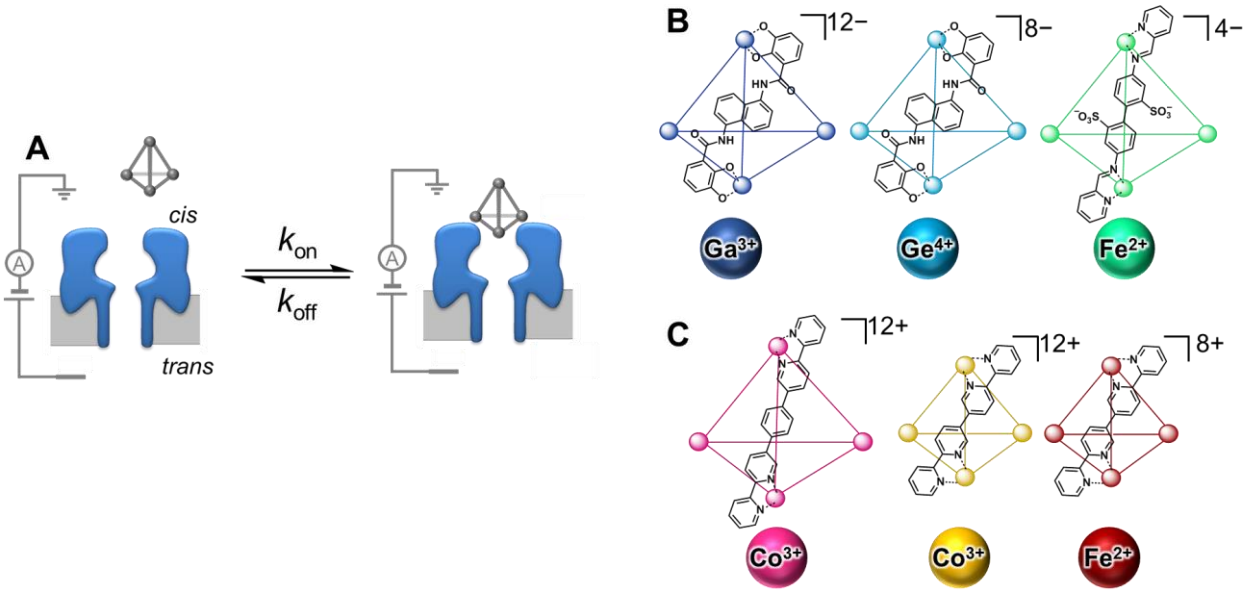

Figure 1. Experimental setup and tetrahedral coordination cages.
(A) Experimental setup in which tetrahedral coordination cages were detected at the *cis*-opening of a single α-hemolysin (α-HL) nanopore inserted in a lipid bilayer under an applied transmembrane potential. (B) Cages bearing an overall negative charge, (C) Cages bearing an overall positive charge. Cage dimensions are listed in Table 1.

Significantly, Bayley *et. al.* have employed a β-cyclodextrin adapter bound within a genetically modified α-hemolysin nanopore to detect and characterize a diverse range of analytes.[37-40] The binding constants of the analytes with the cyclodextrin in bulk solution at equilibrium typically differ by several orders of magnitude compared to the equivalent binding observed in the presence of the externally applied electric field.[37,41] Thus, understanding the influence of externally applied fields on the binding of analytes with nanopores under field-perturbed conditions is crucial for sensing applications, but may also have wider implications in catalysis, nanoscience and supramolecular chemistry.[42] It is important to note that the effects of an externally applied field in nanopore-based systems are manifested *via* a combination of direct electrophoretic forces and secondary electro-osmotic forces arising from the field-induced flux of electrolyte ions.[43,44] While the voltage-driven translocation of analytes through ion channels has been widely investigated,[45-48] the influence of external fields on larger supramolecular assemblies has not.

We recently demonstrated that externally applied fields can be used to trap individual metallosupramolecular cages against an α-hemolysin nanopore, and that ion current recordings enabled both their supramolecular chirality[35] and the binding of guest molecules within their cavities to be resolved.[36] Notably, the measured association constants of the cage with the nanopore were of the order of 10^8 M^{-1}. We reasoned that such exceptionally high binding constants were due to the perturbed-equilibrium binding of the highly charged 12^- cages by virtue of the externally applied voltage.

Here, we have investigated the role of electrostatic forces in field-perturbed binding by examining nanopore•cage complexes at the single-molecule level. The binding of single cage complexes with an individual α-hemolysin protein nanopore was investigated under a range of applied transmembrane potentials (Figure 1A). A series of tetrahedral cages enabled the systematic variation of the charge on the cages while maintaining a similar shape and size (Figure 1B,C). We examined the influence of the magnitude, sign and density of the charge of the cages on the binding kinetics and the position of the perturbed equilibrium (Figures 2, 3 and 5), and the influence of the externally applied voltage (Figure 6). The binding data were rationalized by a simple model that considered the interplay of the externally applied field and the local (molecular) electrostatic interactions

(Figure 4). The ability of the applied voltage to controllably perturb binding equilibria to select a specific cage complex from a mixture was examined (Figure 7). Finally, enantio-inversion of chiral cages under voltage-driven conditions was demonstrated (Figure 8).

RESULTS AND DISCUSSION

Nanopore analysis of cage complexes

Initially we synthesized a range of water-soluble tetrahedral M_4L_6 coordination cages (Figure 1B,C). The synthesis of the negatively charged cages bearing overall charges of 12^- and 8^- were previously reported by the Raymond group,[49,50] while the similarly sized 4^- cage was previously reported by the Nitschke group.[51] We also designed a series of positively charged cages (Figure 1C) based on a previously reported bis(bipyridine) ligand[52] and a shorter analogue. The cationic cages were synthesized as nitrate salts, enabling water solubility (see SI, Section S2).

Nanopore experiments were conducted using a setup in which a planar lipid bilayer was painted across a 100 μm aperture separating two wells of buffered solution (1 M KCl, 30 mM phosphate, pH 8.0) (Figures 1A, S1, S2). A single α-hemolysin nanopore was introduced into the bilayer, as indicated by the characteristic ionic current flowing through the pore at an applied transmembrane voltage of ±100 mV (I_o, Figure 2). Building on our previous nanopore-analyses of cage complexes,[35,36] each of the cages depicted in Figure 1B,C were added to the *cis*-side of the nanopore (Figure 1A). Characteristic temporal blockages in the recorded ion currents were seen at discrete current levels due to interactions between individual cage complexes and the *cis*-entrance of the nanopore (Figure 2). Negatively charged cages gave rise to blockage events under positive applied potentials, while positively charged cages gave events under negative potentials. In line with our previous observations,[35] the interaction of negatively charged cages with the nanopore revealed two discrete current levels in the range of I_b/I_o = 0.67–0.83 corresponding to the homochiral ΔΔΔΔ and ΛΛΛΛ forms of the cages.[53] The separation of these levels became less pronounced as the extent of the current blockage decreased, which itself decreased with the magnitude of the negative charge on the cage (Figure 2A,B *cf.* 2C, and Figures 3A, S11). Indeed, the chiral forms of the positively charged cages were not resolved due to the small current blockages for such species (I_b/I_o = 0.89–0.93, Figures 2, 3A). Although the magnitudes of ion current blockages are complicated by multiple determining factors,[54] the relatively small current blockages for both cationic and anionic cages indicate that the transient bind of cages occurs at the *cis*-entrance of the nanopore, rather than deep within the pore vestibule.

A series of nanopore analyses were performed in which the concentration of each of the tetrahedral cages was varied. Event and inter-event durations (τ_{off} and τ_{on} respectively) were plotted as frequency-count histograms and fitted to single exponential decay functions (see SI section S4.1). In the situations where such binding events could be resolved, no significant difference between the kinetics of the ΔΔΔΔ and ΛΛΛΛ forms of the 4− (Figures S9-S17) or 12^- cages was observed;[35] consequently events for cage enantiomers were treated together in subsequent analyses. For all cages, τ_{off} was found to be independent of cage concentration, whereas τ_{on} was linearly dependent on concentration (Figure 2, right). These concentration dependencies confirmed the bimolecular nature of the interaction between each tetrahedral cage and the nanopore.[29,55] Thus, the rate constants of dissociation, $k_{off} = 1/\tau_{off}$, and association, $k_{on} = 1/\tau_{on}$[cage], could be determined for each cage (Figures 2, 3B,C).

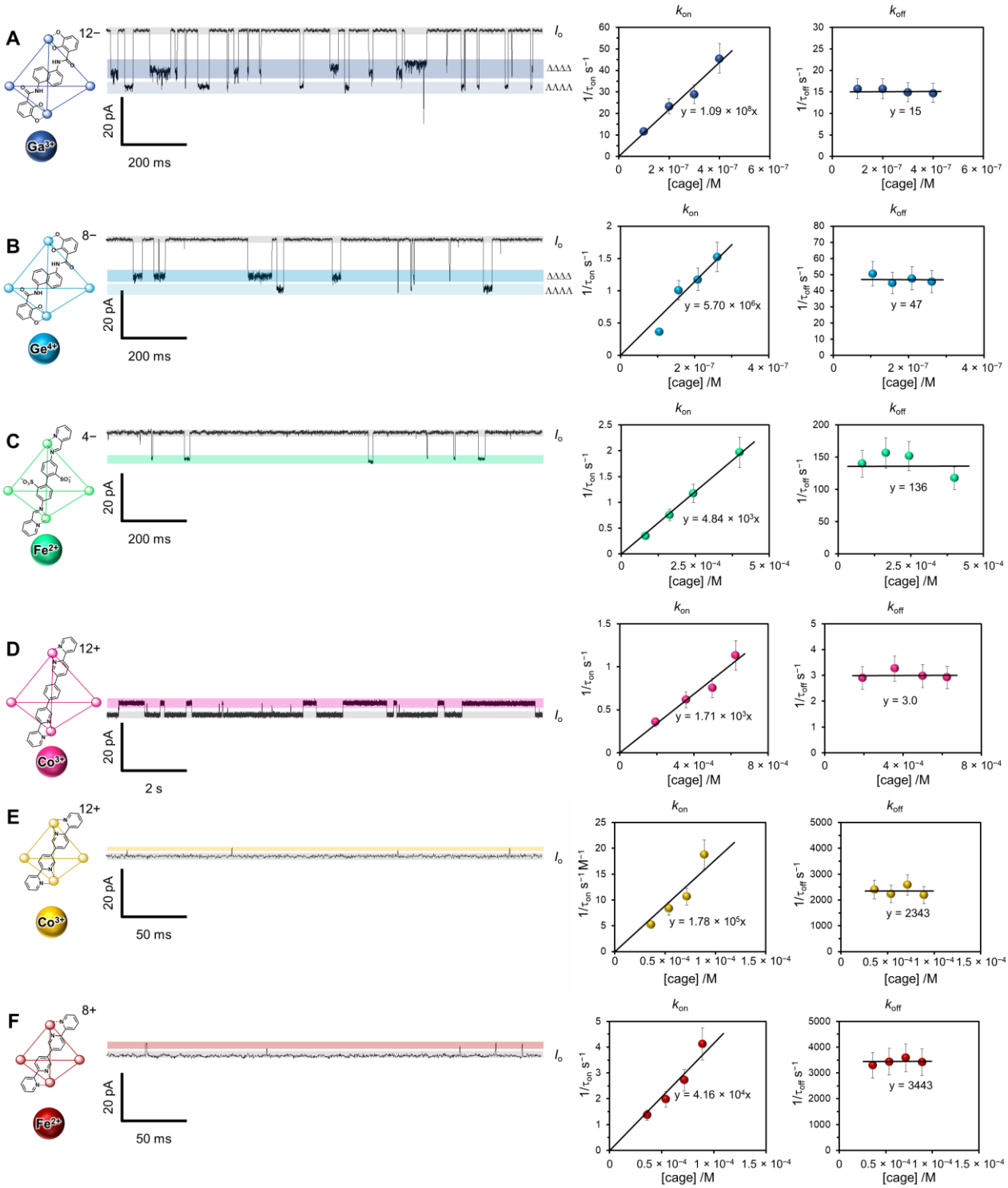

Figure 2. Representative ion current traces and association/dissociation kinetics of cage complexes with an α-HL protein nanopore.

The rate constant k_{on} was obtained from the slope of the linear fit of $1/\tau_{on}$ versus [cage]. The rate constant k_{off} was obtained from the intercept of the graph $1/\tau_{off}$ versus [cage]. Experiments were performed in 1 M KCl, 30 mM Tris.HCl, pD 7.6 (~pH 8.0[56]) in D_2O at 293 ± 2 K with an applied potential of +100 mV (A),[35] 1 M KCl, 30 mM phosphate, pH 8.0 at 293 ± 2 K with an applied potential of +100 mV (B,C) and −100 mV (D–F).

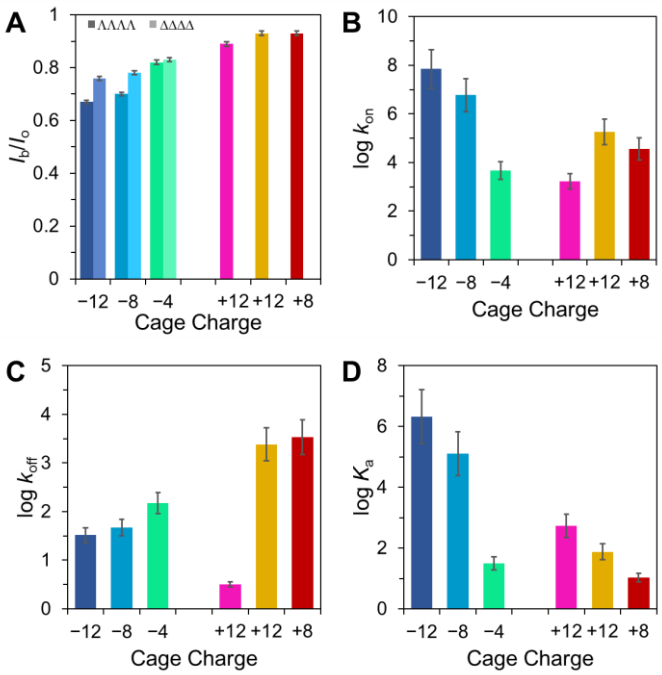

Figure 3. Residual ion currents and field-perturbed binding data.
(A) Residual ion currents, and field-perturbed (B) association rate constants, k_{on} (C) dissociation rate constants, k_{off}, and (D) binding constants, K_a for nanopore•cage complexes determined from nanopore experiments performed in 1 M KCl, 30 mM phosphate,* pH 8.0 at 293 ± 2 K under an applied potential of ±100 mV. *Data for Ga^{3+} 12^- cage obtained in 30 mM Tris buffered D_2O, pD 7.6 (~pH 8.0[56]).[35] All data are provided in Table S1. Distinct data for ΛΛΛΛ and ΔΔΔΔ cage binding events could only be resolved for negatively charged cages.

Both the field-perturbed equilibrium association and dissociation rate constants (k_{on} and k_{off}, respectively, Figure 3B,C) approximately scaled with the magnitude of the charge on each cage at either +100 mV or −100 mV for negatively and positively charged cages, respectively. While k_{on} decreased as the magnitude of the charge on the cages decreased under the same conditions, this trend was inverted for k_{off}. Furthermore, the k_{on} values were both larger and more sensitive to the magnitude of the charge on the cages compared to k_{off}. Accordingly, the field-perturbed equilibrium $K_a = k_{on}/k_{off}$, was also found to decrease as the magnitude of the charge on the cage decreased (Figure 3D). However, these general trends were not always maintained, for example, the larger of the two 12^+-charged cages (pink) appeared to have outlying behavior with regards to both k_{on} and k_{off}, which may be attributed to its larger dimensions, and the associated differences in charge density (*vide infra*).

Rationalizing the patterns in the observed binding kinetics and thermodynamics of these cage•nanopore complexes may help to develop a general understanding of the phenomena governing binding equilibria in nanoscale systems that are perturbed by external fields.

Electrostatic forces in field-perturbed binding equilibria

The binding equilibrium in the present system can be rationalized as being governed by both the force acting on the charged cage as a result of the externally applied electric field (voltage, $E_{applied}$, which will be modulated by secondary electro-osmotic forces) and

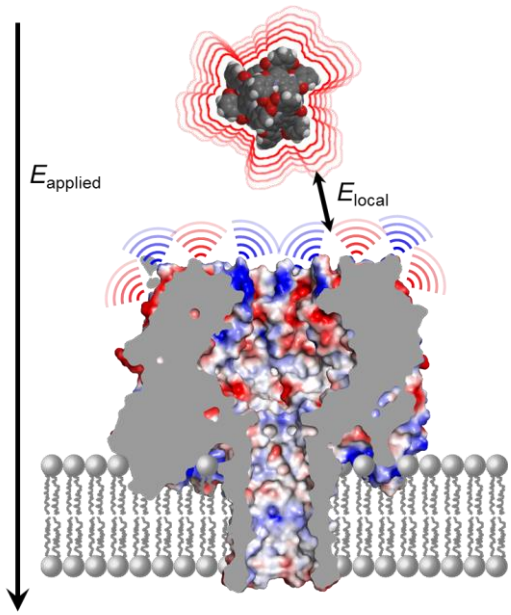

Figure 4. Field-perturbed equilibrium binding of the cage to the pore.
The binding equilibrium of the cage to the pore is determined by the combination of the externally applied electric field (voltage) acting on the cage ($E_{applied}$) and local electrostatic interactions between the cage and the nanopore (E_{local}). Red regions of the surface correspond to negative charge and blue to positive charge. All electrostatic interactions will be further modulated by the solvent and counterions present.

the sum-total of the array of local electrostatic interactions between the cage and the nanopore (E_{local}) (Figure 4). If the force arising from the interaction of the total charge of the cage with the externally applied field was dominant, then it would be expected that the kinetics of binding would be very similar for similarly sized cages that have equal but opposite charges. However, our experimental data show that the negatively charged cages possessed higher k_{on} rates (~2 orders of magnitude), and lower k_{off} rates (~4 orders of magnitude) than the corresponding positively charged cages (Figure 3B,C). While this difference in behavior between the positively and negatively charged cages may be due to the importance of local electrostatic interactions (E_{local}, Figure 4), variations in the sizes of the cages might also modulate the force exerted by the externally applied field ($E_{applied}$, Figure 4). It must be noted that the field across the nanopore is unlikely to be uniform, emphasizing the importance of using similarly sized and shaped cages to ensure comparable binding sites.[57,58] The nanoscale proportions of the cage complexes mean that they are not well described as point charges. The latter size-related aspect can be taken into account by considering the charge density, i.e. the charge per unit volume, rather than the overall charge of the cage. The volume (V) of a tetrahedron is given by Equation 1:

$$V = \frac{a^3}{6\sqrt{2}} \qquad \textbf{Equation 1}$$

Where a is the edge length of the tetrahedral cage, which can be obtained from crystal structures or geometry minimized models of the cages (Figure S3). While metal-metal distances ($Length_{M\text{-}M}$) are often reported in relation to the size of metallosupramolecular assemblies, ligand lengths ($Length_{C\text{-}C}$) that measure the longest carbon-carbon distance on a single ligand provide a better estimate of the dimensions of the cages (Table 1, Figure S3). It should be noted that this calculation assumes a uniform charge distribution, which due to the symmetry of the cages is a reasonable approximation (Figure S5). Using these dimensions allows the experimental k_{on} and k_{off} values to be plotted against the magnitude of the charge density of the cage (Figure 5), obtained by dividing the charge by the volume.

Table 1. Cage dimensions and volumes determined from crystal structures[50,51] or modelled using the Molecular Mechanics Force Field. Lengths between metal centres ($Length_{M\text{-}M}$) and those between the

outermost carbons of the ligand molecules (Length$_{C\text{-}C}$) were used to calculate the corresponding volumes (see SI Figure S3) and charge densities expressed as atomic charge (q) per Ångstrom cubed.

Cage	Length$_{M\text{-}M}$ /Å	Length$_{C\text{-}C}$ /Å	Volume$_{C\text{-}C}$ /Å^3	Charge density /q·Å^{-3}
12−	13.0	16.3	510	−0.024
8−	12.9	16.3	510	−0.016
4−	12.9	19.5	874	−0.005
12+	13.3	19.6	887	+0.014
12+	9.3	15.3	433	+0.028
8+	9.4	15.3	433	+0.019

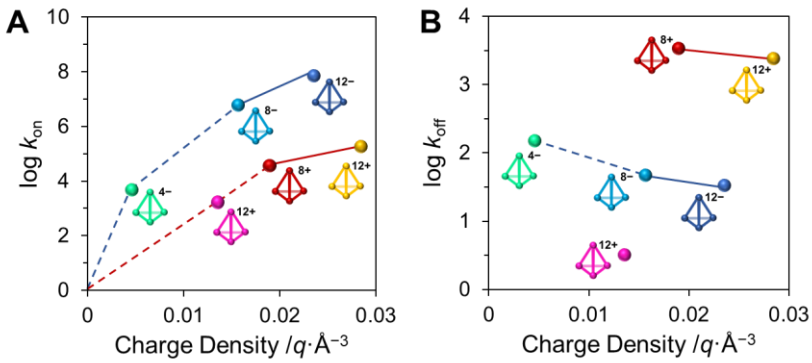

Figure 5. Influence of charge density on the association and dissociation of cage•nanopore complexes.
The magnitude of the charge density of the cages can be determined by dividing the charge by the volume of the cage as determined from the ligand length (Table 1). Charge density is then plotted against the association (A) and dissociation (B) rates obtained at ±100 mV (data from Figure 3). E_{local} is ∝ the charge density.

Strikingly, while the largest 12$^+$ charged cage gave outlying behavior when k_{on} was plotted against the total charge on the cage (pink, Figure 3B), plotting the same experimental data against the charge density gave the pleasing correlation shown in Figure 5A, since the larger 12$^+$ cage actually has a lower charge density than the 8$^+$ cage. Now, the trend of increasing k_{on} with increasing charge density is clear across both series of positively and negatively charged cages. At equivalent charge densities, the k_{on} values of the negatively charged series were approximately three orders of magnitude higher than the positively charged series. Similarly, k_{off} decreased with increasing charge density for both series of cages (with exception of the 12$^+$ cage) and were approximately two orders of magnitude lower for the negatively charged series than the positively charged series at equivalent charge densities (Figure 5B). Despite the improved correlations between the kinetic data and the charge densities of the cages, the non-linear correlations indicate that the rates are not directly proportional to the charge density and therefore the association is not completely dominated by the applied electric field ($E_{applied}$, Figure 4). In addition, the largest 12$^+$ cage (pink) remains a distinct outlier in Figure 5B. Together, these findings indicate that the combination of the force exerted by the applied electric field ($E_{applied}$) and the local electrostatic interactions (E_{local}) between the nanopore and each of the cages both play a significant role in determining the binding kinetics.

An indication of the local electrostatic interactions can be obtained by visualizing the surface charges of the α-hemolysin protein nanopore and the electrostatic potentials of the cages.[54] The nanopore was calculated[59-61] to have a net charge of +7.0 at pH 8.0 that is distributed non-homogeneously over the protein (Figure 4 and S4). Meanwhile, the charges on the cages are both more intense and relatively homogenous (Figure S5). The α-hemolysin bears a ring of positive charge around the *cis*-entrance to the pore, which might account for the higher k_{on} and lower k_{off} of the negatively charged cages (Figure S4).[57,62,63] In contrast to the simple behavior of k_{on}, the k_{off} values appear to be more susceptible to the small variations in the specific shape and size of the individual cages. This situation is well exemplified by the different k_{off} values of the large and small 12^+ cages (pink and yellow respectively, Figure 5). It can be reasoned that the smaller cage enters deeper into the nanopore than the larger cage, and thus experiences a greater repulsion from the positively charged ring of lysine residues at the *cis*-entrance (Figure 4, S4, *cf*. S5). Nonetheless, given the intensity of the charge on the cages, the force exerted on the cages by the externally applied field ($E_{applied}$) will also be a major factor in governing the association/dissociation kinetics.

To examine the effect of changing $E_{applied}$, a second series of nanopore experiments with each of the cage complexes was performed, in which the applied transmembrane potential was varied (see SI section S4.2). Due to the bimolecular nature of the pore•cage complex, the k_{on} and k_{off} values for each cage over a range of voltages could be estimated as above from $k_{off} = 1/\tau_{off}$, and $k_{on} = 1/\tau_{on}$[cage] (Figures S24–S42). The association and dissociation rates were plotted against the magnitude of the applied voltage (Figure 6A–D).

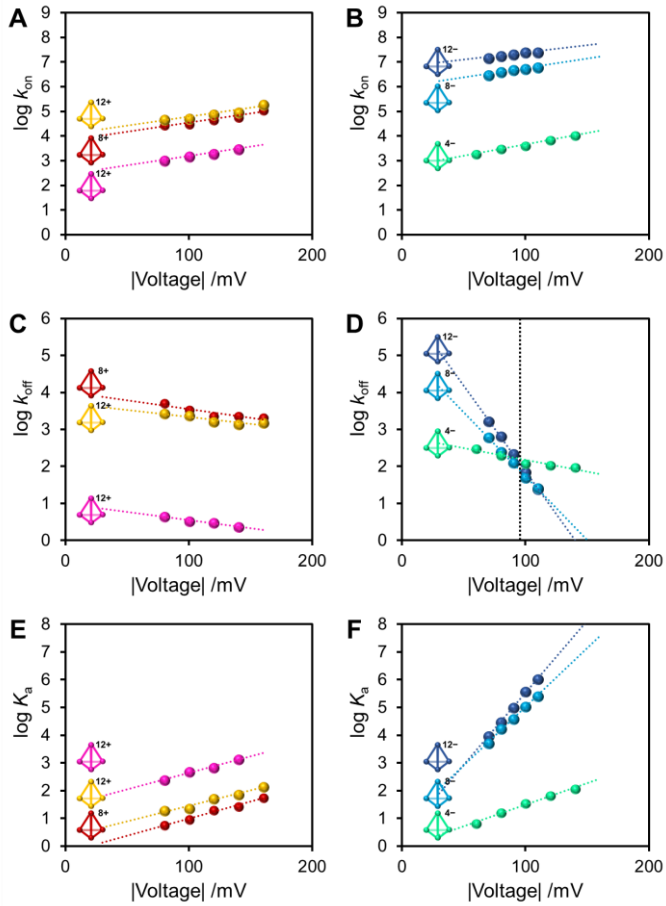

Figure 6. Field-perturbed equilibrium kinetic and thermodynamic data for nanopore•cage complexation.
Kinetic (A–D) and thermodynamic (E), (F) data determined in 1 M KCl, 30 mM phosphate, pH 8.0 at 293 ± 2 K as the applied potential was varied. The dotted vertical line in (D) corresponds to the point at which $E_{applied} \approx E_{local}$. $E_{applied}$ is ∝ the applied voltage.

For all cages, there was a linear relationship between the applied voltage and both log k_{on} and log k_{off}. The values of log k_{on} and k_{off} were respectively directly and inversely proportional to the magnitude of the applied voltage. Strikingly, the values of log k_{on} varied with approximately the same gradient for each of the six cage complexes (Figure 6A,B), further supporting the dominance of $E_{applied}$ in determining the k_{on} rate. The relationship between the magnitude of the applied voltage and the log k_{off} values was more complicated (Figure 6C,D). The gradient of the plots in Figure 6C were similar for all positively charged cages, but the rates were very different for the large (pink) and small (red, yellow) cages. For the negatively charged cages, the gradients in Figure 6D became steeper with increasing negative charge of the cage. This results in a surprising situation where at low applied voltages, the most highly charged 12^- and 8^- cages displayed the highest k_{off} rates, while at higher applied voltages, the opposite situation was observed. E_{local} therefore dominates the k_{off} rate of these cages at lower applied voltages, while the applied field $E_{applied}$ dominates at higher voltages. The voltage at which the correlations for each of the negatively charged cages intersect at +95 mV in Figure 6D corresponds to the point where E_{local} is approximately equal to $E_{applied}$. Interpreting this different behavior is difficult, since multiple factors may be involved. However, the 12^- and 8^- cages have more flexible ligands, while also having slightly different geometries to the other cages examined (Figure S3). Thus, different dynamics and electrostatic interactions may be involved with these cages compared to the others. Despite these differences, it is important to note that the voltage-dependence of the k_{on} for the 12^- and 8^- cages are consistent with the other cages, and thus, the key findings

that association rates are dominated by the externally applied field, while local electrostatic interactions play a more important role in dissociation rates still hold.

The values of the field-perturbed equilibrium association constants, K_a (= k_{on}/k_{off}), increased linearly with increased applied potential (Figure 6E,F). Due to the excellent linear fits, the data could be extrapolated to obtain binding constants and energies at zero applied voltage, *i.e.* under non-perturbed equilibrium conditions (Figure S43C). All the cages displayed negligible or very low binding constants, with the large 12^+ cage (pink) possessing the strongest binding under extrapolated equilibrium conditions in the absence of an electric field, K_a = 28 M^{-1} or ΔG = −8 kJ mol^{-1} at 293 K. These observations indicate the dominance of electrostatic forces in the binding of these highly charged species under applied potentials, which take precedence over desolvation, hydrophobic interactions and other intermolecular interactions that otherwise govern binding in the absence of a perturbing externally applied field. Indeed, the findings underscore the importance of the electric field in perturbing the binding equilibrium such that low concentrations of otherwise weakly binding analytes can be detected in nanopore sensing.

The voltage dependency of K_a, k_{on} and k_{off} in nanopore binding events can also be used to estimate the fractional extent of entry into the electric field.[64,65] Analysis of the data by this approach (Figure S43), gave an average of 11% fractional entry of the cages into the nanopore, consistent with cage binding occurring at the *cis*-entrance of the pore. However, it should be cautioned that this approach requires assumptions to be made about the magnitude of the charges on the cage complexes. Indeed, the differences in the voltage-sensitivity of association and dissociation processes (Figures 6A–D and S43), and therefore the determined fractional entry values, may arise from such differences in counterion involvement and solvation.

Exploiting field-perturbed binding equilibria: selection of cage binding from a mixture

Having quantified the influence of the externally applied electric field on the kinetics and thermodynamics of binding of differently charged cages, we then set out to establish whether such effects could be exploited as a means for gaining external control over binding at the molecular level. Figure 7 depicts an experiment in which a mixture of 1 μM of 8^- cage and 157 μM of 4^- cage were added to a single nanopore experiment. At low voltages, binding of 4^- cage dominated (Figures 7A and S44), as would also be expected under equilibrium conditions in which no electric field was applied. However, at +150 mV it was possible to select for 96% binding of the 8^- cage, despite the >150 equivalent excess of 4^- cage that was also present (Figures 7C and S44).

The main origin of this remarkable ability to tune binding selectivity on varying the externally applied field arises from the differences in the voltage-dependency of the dissociation kinetics; k_{off} changed by 4 orders of magnitude on going from +50 mV to +150 mV for the 8^- cage, but less than 1 order of magnitude for the 4^- cage over the same voltage range (Figure 6D). Indeed, the observed difference in the voltage-sensitivity can be rationalized by the smaller, most charge-dense cage being most greatly influenced by the external field (Figure S43). The net result was that the binding durations of the 8^- cage were dramatically increased at higher voltages relative to the 4^- cage (Figure S44). While both cages had mean binding durations of ~1–2 ms at +50 mV, at +150 mV this increased to ~500 ms for the 8^- cage, but only ~20 ms for the 4^- cage). This voltage-dependent switching underscores the utility gained in understanding the influence of external fields on single-molecule binding equilibria. It also illustrates the capacity to influence molecular recognition events at the single-molecule level using an external stimulus.

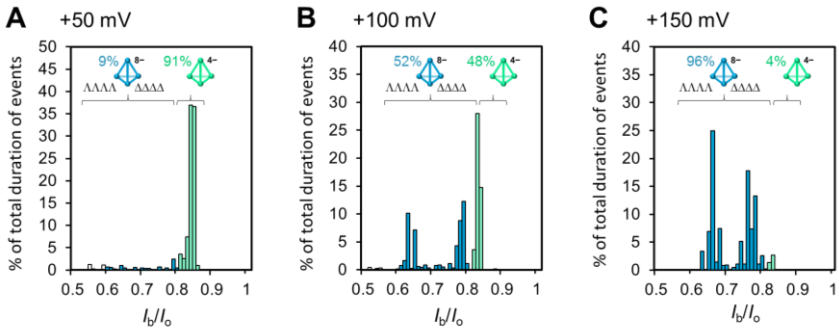

Figure 7. Voltage-based selection of cage binding from a mixture of 1.0 μM of the 8⁻ cage (blue) and 157 μM of the 8⁻ cage (green). Percentage of the total duration of events at each respective residual current bin at A: +50 mV; B: +100 mV; and C: +150 mV applied transmembrane potential. Data determined in 1 M KCl, 30 mM phosphate, pH 8.0 at 293 ± 2 K.

Voltage-driven enantio-inversion of cage complexes and non-equilibrium capture/disassembly

The experiments described in the previous section also revealed more complicated ion current signatures (Figure S44). To examine these events further, additional recordings of the 8⁻ cage alone at +120 mV were performed (Figures 8 and S27B). From a sample of 1150 cage binding events, most exhibited stable on/off current levels consistent with those observed a lower voltages (Figure 8A, left). However, a substantial proportion of events also contained transient meta-stable intermediate states with a reproducibly higher residual current blockage $I_b/I_o \approx 0.54$ (Figure 8A, S27B and S28 green band). Most of these meta-stable states returned to the cage-bound current level from which they originated (ΔΔΔΔ or ΛΛΛΛ, Figure 8B). Strikingly, 38% of the meta-stable ΔΔΔΔ events (14% of all ΔΔΔΔ events) proceeded to the ΛΛΛΛ current level, and 29% of the meta-stable ΛΛΛΛ events (8% of all ΛΛΛΛ events) proceeded to the ΔΔΔΔ current level. Moreover, both types of transition appeared to proceed *via* the same intermediate current level (green band in Figures 8, S27B and S28). While enantio-inversion events have previously been observed in small molecules covalently bound within a nanopore,[66] the implication here is that the electric field (and any induced electro-osmotic forces) acting on the cage enantiomers at higher voltages provides an energy input that enables the barrier to supramolecular enantio-inversion to be overcome. Indeed, careful inspection of ion current traces obtained for the 8⁻ cage at the lower voltage of +80 mV contained less than 0.2% enantio-inversion events (5 in 3285).

The ΔΔΔΔ cage-binding events display more meta-stable states that the ΛΛΛΛ events. This greater number of meta-stable states in turn lead to more enantio-inversion events (Figure 8B). This imbalance between the two capsule enantiomers is likely due to the diastereotopic relationship between the chiral cage and the chiral protein pore.[35] Enantio-inversion of germanium and gallium tris-catecholate complexes is known to occur *via* non-dissociative mechanisms that involve either a trigonal or rhombic twist.[67] The observation that enantio-inversion was always seen to proceed *via* an intermediate (green band in Figure 8 and S27B) rules out a fully concerted mechanism in which each metal centre inverts simultaneously *via* a trigonal twist.

The rates of such isomerization processes tend to increase with the ionic radius of the metal.[67] However, although a very small number of events involving enantio-inversion (2 in 988) were observed for the 12⁻ gallium cage at +110 mV (Figure S24), they occurred less frequently than for the 8⁻ germanium cages despite being constructed from the same cage-forming ligands. Rather than entering a single intermediate current level, as was seen for the germanium cage, the more labile gallium cages instead displayed deeper current blockages at applied potentials of +110 mV and above (Figure S24B). Several of these

deeper blockages persisted for tens of seconds, and in some cases such states could only be escaped by reversing the applied potential. These longer-duration deep blockages may be attributed to kinetically trapped non-equilibrium states in which the applied electric field drives the dissociation of one or more ligands to enable deeper entry and trapping within the pore vestibule. Furthermore, such deeper blockages were occasionally seen to transition directly to an unblocked pore from a deeply blocked state, which would be consistent with non-equilibrium disassembly and transport across the membrane in the direction of the applied electrostatic force (Figure S24B).

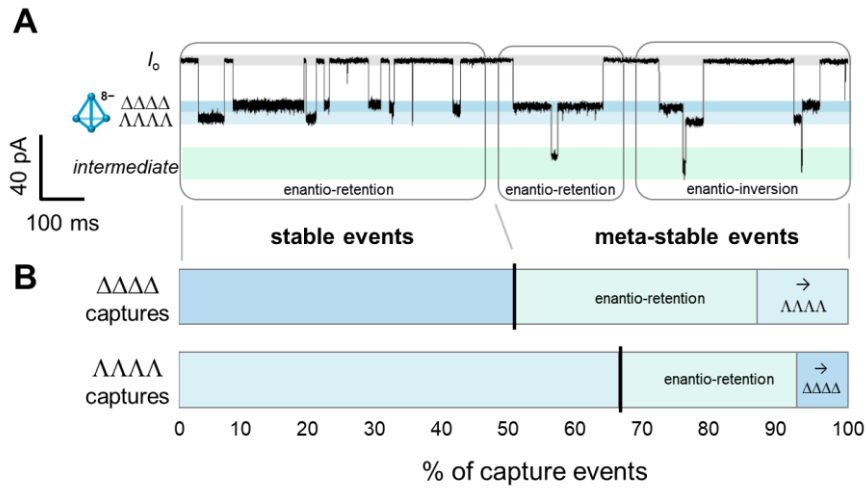

Figure 8. Stereochemical reconfiguration of cage complexes during nanopore association.
A: Ion current traces obtained +120 mV in the presence of 532 nM Ge^{4+} cage contained additional meta-stable and stereochemical inversion events that were not observed at lower applied voltages. B: Distribution of event types from 1154 capture events (n = 2) revealed that the ΔΔΔΔ capture events were less stable than ΛΛΛΛ captures and were more likely to proceed via a meta-stable state to stereochemical inversion. Data obtained in 1 M KCl, 30 mM phosphate in H_2O, pH 8.0, 298 K with 532 nM of the Ge^{4+} cage.

Conclusions

In conclusion, we have investigated the effects of electrostatic forces in field-perturbed binding equilibria. We have examined the voltage-driven association of a series of tetrahedral coordination cages with an α-hemolysin nanopore at the single-molecule level. The single-molecule nature of the approach facilitated direct observation of the influence of the external field on binding kinetics, and thereby thermodynamics. We were able to systematically vary the applied electric field and the charge of the cage, and found that both factors contributed to binding. The association rate, k_{on}, was dominated by the externally applied electric field, resulting in consistent behaviour across all six cages. In contrast, the dissociation rate, k_{off} was dominated either by local or applied forces depending on the nature of the cage and the voltage applied. By exploiting these principles, it was demonstrated that switching the externally applied voltage could be used to select the binding of a specific cage from a mixture, even in the presence of a large excess of another cage. Indeed, we hope that our finding that association rates are dominated by the external field, while local effects are more likely to play a role in determining the dissociation rates may prove to be both general and transferrable, since this provides a readily accessible means of controlling molecular recognition events using an external stimulus. Moreover, higher applied voltages (>110 mV) were shown to provide a driving force that enabled enantio-inversion of the germanium-based cages *via* an intermediate metastable state. Due to the diastereotopic relationship between the chiral protein pore and the cages, this voltage-mediated process contributes towards shifting the population of the two enantiomers away from the initial racemic population, and thereby constitutes a novel form of dynamic kinetic resolution. In contrast, the closely related, but more labile gallium cages also displayed enantio-inversion events at the same applied potential, but were more likely to enter kinetically trapped states consistent with partial disassembly leading to deeper entry or translocation through the pore. While such non-equilibrium situations are

particularly challenging to predict *a priori*, we hope that the general principles relating to field-perturbed equilibria (specifically, the influences of electric fields on association and dissociation kinetics) will aid the design of molecular devices that operate within externally applied electric fields or biogenic transmembrane potentials.[68] However, to date there is a paucity of systematic experimental investigations of electrostatic forces in nanoscale systems, and thus we also hope to encourage similar quantitative fundamental investigations of this emerging area.

EXPERIMENTAL PROCEDURES

Synthesis of novel cage complexes

Small Co^{3+} cage: Cobalt nitrate hexahydrate (21.1 mg, 72.5 μmol) and ligand **S1** (33.7 mg, 109 μmol) were suspended in a mixture of degassed H_2O/MeCN (9:1 *v*/*v*, 5.0 mL) and heated at 50 °C for 15 h under N_2. The reaction was cooled to room temperature and cerium(IV) ammonium nitrate (59.8 mg, 109 μmol) in MeCN (6.6 mL) was added *via* syringe pump (6 μL min^{-1}, 18 h). Dilution with MeCN (8.0 mL) was required to precipitate the product, which was isolated by filtration onto celite and washed with further MeCN. The product was eluted with water, and the solution was freeze-dried to give the desired product as a yellow solid (42.0 mg, 14.9 μmol, 82%). ^{1}H NMR (500 MHz, D_2O): δ = 8.97 (d, *J* = 8.1 Hz, 12H), 8.81 (d, *J* = 8.4 Hz, 12H), 8.62 (dd, *J* = 8.1, 7.0 Hz, 12H), 7.91 (d, *J* = 8.4 Hz, 12H), 7.83 (dd, *J* = 7.0, 6.0 Hz, 12H), 7.62 (d, *J* = 6.0 Hz, 12H), 7.50 (s, 12H). ^{13}C NMR (126 MHz, D_2O): δ = 155.8, 154.6, 151.7, 149.2, 144.5, 144.5 138.2, 131.8, 127.9, 126.5. ^{1}H DOSY NMR (500 MHz, D_2O): *D* = 2.17 × 10^{-6} cm^2 s^{-1}; calculated hydrodynamic radius = 11.3 Å. ESI-MS (*m/z*): 885 (3+), 648 (4+), 344 (7+), 293 (8+).

Small Fe^{2+} cage: $Fe(ClO_4)_2$•$2H_2O$ (58.2 mg, 0.20 mmol) and ligand **S1** (93.1 mg, 0.30 mmol) were suspended in CH_3CN (8.0 mL) and stirred at 50 °C for 2 hours. Tetramethyl ammonium nitrate (544 mg, 4.0 mmol, 20 eq.) was added and stirred for 10 mins. The resultant precipitate was collected under vacuum filtration, washed with CH_3CN (4 × 10.0 mL) and dried with Et_2O (4 × 10.0 mL) to give the desired compound as a red powder (97.1 mg, 0.038 mmol, 75%). ^{1}H NMR (500 MHz, D_2O/CD_3CN, 12:1 *v*/*v*) δ = 8.79 (d, J = 8.2 Hz, 12H), 8.62 (d, J = 8.3 Hz, 12H), 8.27 (app. t, J = 7.9 Hz, 12H), 7.82 (d, J = 5.4 Hz, 12H), 7.51 (app. t, J = 6.6 Hz, 12H), 7.44 (d, J = 8.3 Hz, 12H), 7.23 (s, 12H). ^{13}C NMR (126 MHz, D_2O/CD_3CN, 12:1 *v*/*v*) δ = 160.0, 158.8, 155.4, 152.8, 139.9, 139.4, 136.6, 128.4, 125.4, 123.7. ESI-MS (m/z): 1229 (2+), 798 (3+), 583 (4+).

Large Co^{3+} cage: Cobalt nitrate hexahydrate (8.4 mg, 28.9 μmol) and ligand **S2** (16.8 mg, 43.5 mmol) were suspended in a mixture of degassed H_2O/MeCN (9:1 *v*/*v*, 5.0 mL) and heated at 50 °C for 1 h under N_2. The reaction was cooled to room temperature before cerium(IV) ammonium nitrate (23.9 mg, 44.0 μmol) in MeCN (0.75 mL) was added *via* syringe pump (25 μL min^{-1}, 0.5 h). Some turbidity was observed, but dilution with MeCN (20 mL) was required to precipitate the product, which was isolated by filtration onto celite and washed with further MeCN. The product was eluted with water and the solution was freeze-dried to give the desired product as a yellow solid (23.1 mg, 7.03 μmol, 97%). ^{1}H NMR (500 MHz, D_2O): δ = 9.00 (d, *J* = 8.6 Hz, 12H), 8.91 (d, *J* = 8.1 Hz, 12H), 8.85 (dd, *J* = 8.6, 1.5 Hz, 12H), 8.58 (dd, *J* = 8.1, 7.0 Hz, 12H), 7.83 (dd, *J* = 7.0, 6.0 Hz, 12H), 7.59 (d, *J* = 1.5 Hz, 12H), 7.5 (d, *J* = 6.0 Hz, 12H), 7.35 (s, 24H). ^{13}C NMR (126 MHz, D_2O): δ = 155.4, 154.4, 151.1, 148.0, 144.1, 141.9, 141.6, 134.5, 131.2, 127.6, 127.3, 126.8. ^{1}H DOSY NMR (500 MHz, D_2O): *D* = 1.56 × 10^{-6} cm^2 s^{-1}; calculated hydrodynamic radius = 15.8 Å.

Single channel experiment set up

Single channel experiments were performed in a custom-built cell (Figure S1, S2 and associated text). A hanging drop of hexadecane in *n*-pentane (5 μL, 10%, *v*/*v*) was touched on each side of the Teflon sheet containing an aperture and allowed to dry for 1 minute. KCl/potassium phosphate buffer (600 μL) was added to the well each side of the aperture. Lipid (1,2-diphytanoyl-*sn*-glycero-3-phosphocholine) (approx. 8 μL, 10 μg $μL^{-1}$) was added to each side of the well, and left for approx. 5 mins to allow the pentane to evaporate The cell was subsequently placed into a Faraday cage and Ag/AgCl electrodes (Warner), connected

to a patch clamp amplifier (Axopatch 200B, Molecular Devices), were suspended either side of the Teflon sheet. The buffer solution on both sides of the Teflon sheet was aspirated and dispensed using a Hamilton syringe to 'paint' a phospholipid bilayer across the aperture. A ±1 mV pulse was applied at 1333 Hz to determine when a bilayer was obtained (capacitance of 40 to 70 pF). The membrane was characterized with successive 2 second sweeps under an applied potential ranging from +100 to −100 mM (Figure S6). The membrane was deemed acceptable if the range of current flow across the membrane measured <1 pA. A gel loading tip fitted to a 20 μL pipette was introduced into an aqueous solution of α-HL (approx. 250 μM (5 μL of the storage solution diluted with 45 μL of water)), without aspirating, such that a tiny amount (<1 μL) of the solution remained on the tip. The α-HL was then fired at the aperture. If after 10 minutes, no channel insertion was observed, then this process was repeated until a single channel arose (Figure S6).

Fixed voltage cage titrations

A stock solution of each cage complex was made up in D_2O (the small Fe^{2+} cage required ~8% CD_3CN and the Ga^{3+} cage required 2 μL of 2 M KOH to ensure good solubility). The concentration of the stock solution was determined against an internal standard (^{i}PrOH) by ^{1}H NMR spectroscopy (500 MHz, 298 K). Cage concentrations were generally 0.5–5 mM. An appropriate volume (generally 5–50 μL) of the stock solution was added to the *cis*-side of the membrane under a ±100 mV applied potential, as appropriate based on the charge on the cage. Data generally totalling >1000 cage binding events was collected at each concentration across a range of experiments. All data were collected using the patch clamp amplifier, and digitized (Axon Instruments Digidata 1332A) at a sample rate of 50 kHz. Single-channel ion current recordings were processed with Clampex 10.2 and Clampfit 10.2 software. All data was recorded at +/−100 mV in 100 second sweeps. At the start and end of each sweep the applied potential was reduced to 0 mV.

Variable voltage cage experiments

An appropriate volume (generally 5–50 μL) of the stock solution of the cages was added to the *cis*-side of the membrane. The applied voltage was varied and data generally totalling >500 cage binding events was collected at each voltage. All data were collected using the patch clamp amplifier, and digitized (Axon Instruments Digidata 1332A) at a sample rate of 50 kHz. Single-channel ion current recordings were processed with Clampex 10.2 and Clampfit 10.2 software. All data was recorded at +/−100 mV in 100 second sweeps. At the start and end of each sweep the applied potential was reduced to 0 mV.

Data processing

Single-channel ion current recordings were processed with Clampex 10.2 and Clampfit 10.2 software. Data was baseline corrected and filtered with a Lowpass Bessel (8-pole) filter with a 200 or 50 Hz cut-off for trace presentation and single-channel analysis respectively. The traces were then analysed with a threshold protocol. The results of the single-channel search were exported into Microsoft Excel 2013 for further processing, such as excluding certain levels. Exponential decays were fitted iteratively using the solver package to minimize the residuals between fitted and experimental data. Standard errors of 10% were applied to the values of k_{on} and k_{off}, and a corresponding propagated error of 14% for K_a values in line with our previously reported measurements.[35]

SUPPLEMENTAL INFORMATION

Supplemental Information contains experimental procedures, additional data, and modeled structures. (PDF)

ACKNOWLEDGMENTS

We thank the Edinburgh Protein Purification Facility for equipment access and ERC Starting Grant 336935, "Transmembrane molecular machines" for funding. EKB and PJL thank the EPSRC for funding grant EP/P025986/1. This work was supported by the Leverhulme Trust (RPG-2015-232).

AUTHOR CONTRIBUTIONS

The manuscript was written through the contribution of all authors. MJB, AS, WG, JVN synthesized cage complexes, SB, MMH, SO and JAC performed nanopore analysis. EKB, PJL and SLC devised the project.

DECLARATION OF INTERESTS

The authors declare no competing interests.

REFERENCES AND NOTES

1. Lehn, J.-M. (1995). Supramolecular Chemistry (VCH).
2. Lehn, J.-M. (2017). Supramolecular chemistry: Where from? Where to? Chem. Soc. Rev. *46*, 2378-2379.
3. Huang, F., and Anslyn, E.V. (2015). Introduction: Supramolecular Chemistry. Chem. Rev. *115*, 6999-7000.
4. Prins, L.J., Reinhoudt, D.N., and Timmerman, P. (2001). Noncovalent synthesis using hydrogen bonding. Angew. Chem. Int. Ed. *40*, 2382-2426.
5. Ma, X., and Zhao, Y. (2015). Biomedical applications of supramolecular systems based on host–guest interactions. Chem. Rev. *115*, 7794-7839.
6. Liu, Y., Sengupta, A., Raghavachari, K., and Flood, A.H. (2017). Anion binding in solution: beyond the electrostatic regime. Chem *3*, 411-427.
7. van Esch, J.H., Klajn, R., and Otto, S. (2017). Chemical systems out of equilibrium. Chem. Soc. Rev. *46*, 5474-5475.
8. Mattia, E., and Otto, S. (2015). Supramolecular systems chemistry. Nat. Nanotechnol. *10*, 111.
9. Amos, L.A. (2008). Molecular motors: not quite like clockwork. Cell. Mol. Life Sci. *65*, 509.
10. Schliwa, M., and Woehlke, G. (2003). Molecular motors. Nature *422*, 759.
11. Vale, R.D. (2003). The molecular motor toolbox for intracellular transport. Cell *112*, 467-480.
12. Vale, R.D., and Milligan, R.A. (2000). The way things move: Looking under the hood of molecular motor proteins. Science *288*, 88-95.
13. Hammond, C. (2015). Chapter 3 - Ionic gradients, membrane potential and ionic currents. In Cellular and Molecular Neurophysiology, C. Hammond, ed. (Boston: Academic Press), pp. 39-54.
14. Kassem, S., van Leeuwen, T., Lubbe, A.S., Wilson, M.R., Feringa, B.L., and Leigh, D.A. (2017). Artificial molecular motors. Chem. Soc. Rev. *46*, 2592-2621.
15. Erbas-Cakmak, S., Leigh, D.A., McTernan, C.T., and Nussbaumer, A.L. (2015). Artificial molecular machines. Chem. Rev. *115*, 10081-10206.
16. Kay, E. R., Leigh, D. A., Zerbetto, F. (2007). Synthetic molecular motors and mechanical machines. Angew. Chem. Int. Ed. *46*, 72-191.
17. Kay, E. R., Leigh, D. A. (2015). Rise of the molecular machines. Angew. Chem. Int. Ed. *54*, 10080-10088.
18. van Rossum, S.A.P., Tena-Solsona, M., van Esch, J.H., Eelkema, R., and Boekhoven, J. (2017). Dissipative out-of-equilibrium assembly of man-made supramolecular materials. Chem. Soc. Rev. *46*, 5519-5535.
19. della Sala, F., Neri, S., Maiti, S., Chen, J.L.Y., and Prins, L.J. (2017). Transient self-assembly of molecular nanostructures driven by chemical fuels. Curr. Opin. Biotechnol. *46*, 27-33.
20. Hess, H., and Ross, J.L. (2017). Non-equilibrium assembly of microtubules: from molecules to autonomous chemical robots. Chem. Soc. Rev. *46*, 5570-5587.
21. Sorrenti, A., Leira-Iglesias, J., Markvoort, A.J., de Greef, T.F.A., and Hermans, T.M. (2017). Non-equilibrium supramolecular polymerization. Chem. Soc. Rev. *46*, 5476-5490.
22. Pezzato, C., Cheng, C., Stoddart, J.F., and Astumian, R.D. (2017). Mastering the non-equilibrium assembly and operation of molecular machines. Chem. Soc. Rev. *46*, 5491-5507.
23. Beatus, T., Shani, I., Bar-Ziv, R.H., and Tlusty, T. (2017). Two-dimensional flow of driven particles: a microfluidic pathway to the non-equilibrium frontier. Chem. Soc. Rev. *46*, 5620-5646.
24. Bayley, H., and Cremer, P.S. (2001). Stochastic sensors inspired by biology. Nature *413*, 226.
25. Schmidt, J. (2005). Stochastic sensors. Journal of Materials Chemistry *15*, 831-840.
26. Tsutsui, M., Taniguchi, M., Yokota, K., and Kawai, T. (2010). Identifying single nucleotides by tunnelling current. Nat. Nanotechnol. *5*, 286.
27. Ying, Y.-L., Li, Z.-Y., Hu, Z.-L., Zhang, J., Meng, F.-N., Cao, C., Long, Y.-T., and Tian, H. A Time-resolved single molecular train based on aerolysin nanopore. Chem.
28. Song, L., Hobaugh, M.R., Shustak, C., Cheley, S., Bayley, H., and Gouaux, J.E. (1996). Structure of staphylococcal α-hemolysin, a heptameric transmembrane pore. Science *274*, 1859-1865.

29. Kang, X.-f., Cheley, S., Guan, X., and Bayley, H. (2006). Stochastic detection of enantiomers. J. Am. Chem. Soc. *128*, 10684-10685.
30. Wu, H.-C., and Bayley, H. (2008). Single-molecule detection of nitrogen mustards by covalent reaction within a protein nanopore. J. Am. Chem. Soc. *130*, 6813-6819.
31. Clarke, J., Wu, H.-C., Jayasinghe, L., Patel, A., Reid, S., and Bayley, H. (2009). Continuous base identification for single-molecule nanopore DNA sequencing. Nat. Nanotechnol. *4*, 265.
32. Stoddart, D., Heron, A.J., Klingelhoefer, J., Mikhailova, E., Maglia, G., and Bayley, H. (2010). Nucleobase recognition in ssDNA at the central constriction of the α-hemolysin pore. Nano Lett. *10*, 3633-3637.
33. Ayub, M., Stoddart, D., and Bayley, H. (2015). Nucleobase recognition by truncated α-hemolysin pores. ACS Nano *9*, 7895-7903.
34. Wloka, C., Van Meervelt, V., van Gelder, D., Danda, N., Jager, N., Williams, C.P., and Maglia, G. (2017). Label-free and real-time detection of protein ubiquitination with a biological nanopore. ACS Nano *11*, 4387-4394.
35. Cooper, J.A., Borsley, S., Lusby, P.J., and Cockroft, S.L. (2017). Discrimination of supramolecular chirality using a protein nanopore. Chem. Sci. *8*, 5005-5009.
36. Borsley, S., Cooper, J.A., Lusby P. J., Cockroft, S. L. (2018). Nanopore detection of single-molecule binding within a metallosupramolecular cage. Chem. Eur. J. *24*, 4542-4546.
37. Gu, L.-Q., Braha, O., Conlan, S., Cheley, S., and Bayley, H. (1999). Stochastic sensing of organic analytes by a pore-forming protein containing a molecular adapter. Nature *398*, 686.
38. Wu, H.-C., Astier, Y., Maglia, G., Mikhailova, E., and Bayley, H. (2007). Protein nanopores with covalently attached molecular adapters. J. Am. Chem. Soc. *129*, 16142-16148.
39. Banerjee, A., Mikhailova, E., Cheley, S., Gu, L.-Q., Montoya, M., Nagaoka, Y., Gouaux, E., and Bayley, H. (2010). Molecular bases of cyclodextrin adapter interactions with engineered protein nanopores. Proc. Natl Acad. Sci. USA *107*, 8165-8170.
40. Li, W.-W., Claridge, T.D.W., Li, Q., Wormald, M.R., Davis, B.G., and Bayley, H. (2011). Tuning the cavity of cyclodextrins: Altered sugar adaptors in protein pores. J. Am. Chem. Soc. *133*, 1987-2001.
41. Rekharsky, M.V., and Inoue, Y. (1998). Complexation thermodynamics of cyclodextrins. Chem. Rev. *98*, 1875-1918.
42. Hong, C.M., Morimoto, M., Kapustin, E.A., Alzakhem, N., Bergman, R.G., Raymond, K.N., and Toste, F.D. (2018). Deconvoluting the role of charge in a supramolecular catalyst. J. Am. Chem. Soc. *140*, 6591-6595.
43. Squires, A., and Meller, A. (2013). DNA capture and translocation through nanoscale pores—a fine balance of electrophoresis and electroosmosis. Biophys. J. *105*, 543-544.
44. Huang, G., Willems, K., Soskine, M., Wloka, C., and Maglia, G. (2017). Electro-osmotic capture and ionic discrimination of peptide and protein biomarkers with FraC nanopores. Nat. Commun. *8*, 935.
45. Hille, B. (2001). Ion Channels of Excitable Membranes (Sinauer).
46. Stauffer, D.A., and Karlin, A. (1994). Electrostatic potential of the acetylcholine binding sites in the nicotinic receptor probed by reactions of binding-site cysteines with charged methanethiosulfonates. Biochemistry *33*, 6840-6849.
47. Watson, M.A., and Cockroft, S.L. (2015). DNA modulates solvent isotope effects in a nanopore. Chem. Commun. *51*, 12243-12246.
48. Maglia, G., Restrepo, M.R., Mikhailova, E., and Bayley, H. (2008). Enhanced translocation of single DNA molecules through α-hemolysin nanopores by manipulation of internal charge. Proc. Natl Acad. Sci. *105*, 19720-19725.
49. Caulder, D.L., Powers, R.E., Parac, T.N., and Raymond, K.N. (1998). The self-assembly of a predesigned tetrahedral $M4L_6$ supramolecular cluster. Angew. Chem. Int. Ed. *37*, 1840-1843.
50. Davis, A.V., and Raymond, K.N. (2005). The big squeeze: Guest exchange in an M_4L_6 supramolecular host. J. Am. Chem. Soc. *127*, 7912-7919.
51. Prasenjit, M., David, S., Kodiah, B., Kari, R., and R., N.J. (2008). An unlockable–relockable iron cage by subcomponent self-assembly. Angew. Chem. Int. Ed. *47*, 8297-8301.
52. Burke, M.J., Nichol, G.S., and Lusby, P.J. (2016). Orthogonal selection and fixing of coordination self-assembly pathways for robust metallo-organic ensemble construction. J. Am. Chem. Soc. *138*, 9308-9315.
53. Variations in the current level seen in the ΔΔΔΔ form in Figure 2a relate to the binding of guest within the cage, see Chem. Eur. J., 24, 4542-4546 (2018).
54. Buchsbaum, S.F., Mitchell, N., Martin, H., Wiggin, M., Marziali, A., Coveney, P.V., Siwy, Z., and Howorka, S. (2013). Disentangling steric and electrostatic factors in nanoscale transport through confined space. Nano Lett. *13*, 3890-3896.
55. Orit, B., Jadon, W., Li-Qun, G., Kimoon, K., and Hagan, B. (2005). Carriers *versus* adapters in stochastic sensing. ChemPhysChem *6*, 889-892.

56. Mikkelsen, K., and Nielsen, S.O. (1960). Acidity measurements with the glass electrode in H_2O-D_2O mixtures. J. Phys. Chem. *64*, 632-637.
57. Aksimentiev, A., and Schulten, K. (2005). Imaging α-hemolysin with molecular dynamics: ionic conductance, osmotic permeability, and the electrostatic potential map. Biophys. J. *88*, 3745-3761.
58. Howorka, S., and Bayley, H. (2002). Probing distance and electrical potential within a protein pore with tethered DNA. Biophys. J. *83*, 3202-3210.
59. Anandakrishnan, R., Aguilar, B., and Onufriev, A.V. (2012). H++ 3.0: automating p*K* prediction and the preparation of biomolecular structures for atomistic molecular modeling and simulations. Nuc. Acids Res. *40*, W537-W541.
60. Myers, J., Grothaus, G., Narayanan, S., and Onufriev, A. (2006). A simple clustering algorithm can be accurate enough for use in calculations of p*K*s in macromolecules. Proteins: Structure, Function, and Bioinformatics *63*, 928-938.
61. Gordon, J.C., Myers, J.B., Folta, T., Shoja, V., Heath, L.S., and Onufriev, A. (2005). H++: a server for estimating pK_as and adding missing hydrogens to macromolecules. Nuc. Acids Res. *33*, W368-W371.
62. Wang, Y.-Q., Cao, C., Ying, Y.-L., Li, S., Wang, M.-B., Huang, J., and Long, Y.-T. (2018). Rationally designed sensing selectivity and sensitivity of an aerolysin nanopore via site-directed mutagenesis. ACS Sensors *3*, 779-783.
63. Wang, Y.-Q., Li, M.-Y., Qiu, H., Cao, C., Wang, M.-B., Wu, X.-Y., Huang, J., Ying, Y.-L., and Long, Y.-T. (2018). Identification of essential sensitive regions of the aerolysin nanopore for single oligonucleotide analysis. Anal. Chem. *90*, 7790-7794.
64. Woodhull, A.M. (1973). Ionic blockage of sodium channels in nerve. J. Gen. Physiol. *61*, 687.
65. Sanchez-Quesada, J., Ghadiri, M.R., Bayley, H., and Braha, O. (2000). Cyclic peptides as molecular adapters for a pore-forming protein. J. Am. Chem. Soc. *122*, 11757-11766.
66. Steffensen, M.B., Rotem, D., and Bayley, H. (2014). Single-molecule analysis of chirality in a multicomponent reaction network. Nat.Chem. *6*, 603.
67. Davis, A.V., Firman, T.K., Hay, B.P., and Raymond, K.N. (2006). d-Orbital effects on stereochemical non-rigidity: Twisted TiIV intramolecular dynamics. J. Am. Chem. Soc. *128*, 9484-9496.
68. Watson, M.A., and Cockroft, S.L. (2016). Man-made molecular machines: membrane bound. Chem. Soc. Rev. *45*, 6118-6129.

GRAPHICAL TOC ENTRY